Available online at www.sciencedirect.com
SCIENCE DIRECT®
Physica D 209 (2005) 178–190
PHYSICA D
www.elsevier.com/locate/physd

Contact-line instability of dewetting thin films

A. Münch[a,b], B. Wagner[b,*]

[a] *Humboldt University of Berlin, Institute of Mathematics, 10099 Berlin, Germany*
[b] *Weierstrass Institute for Applied Analysis and Stochastics (WIAS), Mohrenstraße 39, 10117 Berlin, Germany*

Available online 25 July 2005

Abstract

We investigate the linear stability of dewetting thin polymer films on hydrophobised substrates driven by Van-der-Waals forces, using a lubrication model. We focus on the role of slippage in the emerging instability at the three-phase contact-line and compare our results to the corresponding no-slip case. Our analysis shows that generically, small perturbations of the receding front are amplified, but in the slippage case by orders of magnitude larger than in the no-slip case. Moreover, while the perturbations become symmetrical in the no-slip case, they are asymmetrical in the slippage case. We furthermore extend our lubrication model to include effects of nonlinear curvature.

Keywords: Stability; Lubrication Approximation; Slippage

1. Introduction

A thin liquid film that wets a solid substrate is typically subject to contact-line instabilities such as formation of fingers. Such phenomena have been studied for decades, both theoretically and experimentally, for films driven by forces such as gravity [1,14,36,38], or Marangoni stresses or both [2,6,8,10,16]. The derivation of the mathematical models exploits the separation of length scales to obtain a simplified lubrication model from the underlying Navier–Stokes equations in conjunction with conservation of mass. The stress singularity at the three phase contact-line, which is inherited by the resulting fourth order PDE, is regularized for example, via a slip boundary condition or precursor model, where the height of the precursor or the slip length is usually much smaller than the height of the actual wetting film. Interestingly, for the wetting phenomena just mentioned, the choice of the boundary condition at the three phase contact-line enters only weakly in that it does not influence the eventual appearance of fingers,

* Corresponding author.
E-mail address: wagnerb@wias-berlin.de (B. Wagner).

0167-2789/$ – see front matter © 2005 Elsevier B.V. All rights reserved.
doi:10.1016/j.physd.2005.06.027

see for example [1,16,18,22]. In contrast to these wetting phenomena, contact-line instabilities for dewetting thin films have received only limited attention particularly theoretically.

For such a process to occur, a thin, viscous film is uniformly spread onto a hydrophobic surface. It then dewets in a process that is initiated either spontaneously through spinodal decomposition or induced for example through nucleation. The dry spots, or holes, that form as a result subsequently grow as the newly formed contact-line recedes, thereby accumulating liquid in a characteristic capillary ridge at the edge of the hole, which increases in width and height as the dewetting proceeds. In a variety of experimental situations it is observed that, while in some cases, the growth of the hole continues until it collides with neighboring holes, in other cases the ridge of the hole destabilizes into finger-like structures eventually pinching off and forming droplets. A similar scenario has also been observed for straight dewetting fronts as opposed to radially symmetric fronts, see [17,21,24,27,30,33,34,40]. Because of the impact this has on the emerging macroscopic pattern, it is important to understand the dynamics leading to such an instability.

Let us note here that in contrast to the previously mentioned wetting scenarios, the film thickness in dewetting experiments is typically orders of magnitude smaller. For such situations, the relevance of slippage at the liquid/solid interface for the instability has been discussed by several authors, [19,29,35], but detailed theoretical investigations using a fluid mechanical model to understand the effect of slippage have not yet been carried out. In [4,15,25] the dewetting rate and shape of the ridge have been treated using approximate formulas derived from scaling arguments and energy balances. This has been compared to dewetting rates and shapes by numerically solving the corresponding lubrication model, both for the no-slip and slippage case, see [11,20]. In [20] also the case for very hydrophobic substrates is investigated. For such situations contact angles are typically quite large and violate the small slope assumption of lubrication theory, suggesting to include the full nonlinear expression for the curvature of the liquid surface.

In this paper, we study the linear stability of the dewetting ridges, by perturbing about the solutions found in [20]. In Section 2, we describe the relevant physical situation and derive the lubrication model. In Section 3, we discuss the two asymptotic cases: the no-slip case and the slip case for the lubrication model as well as for the extended model that includes nonlinear curvature. Subsequently, we detail the numerical methods used and present our results. In Section 4, we summarize our results.

2. Formulation

2.1. Effective interface potential

The physical situation that underlies our mathematical model consists of a thin viscous polymer film using polystyrene (PS) of low molecular weight ($\sim$5 kg/mol) and about 100–200 nm thick, that is uniformly spread on a substrate, consisting essentially of a silicon wafer (Si) covered with a silicon oxide (SiO) layer, which is in turn covered with a monolayer of octadecyl-trichlorosilane (OTS). For such a multi-layer system, it could be shown in [31,32], how to reconstruct a corresponding effective interface potential. This can then be used to characterize the stability properties of the thin film with respect to spinodal decomposition and nucleation with the aim to extract information for the resulting dewetting pattern.

The effective interface potential is composed of repulsive and attractive long-range Van-der-Waals contributions, with a separate contribution for each of the layers of the substrate, and a short-range term which accounts for Born-type repulsion. The latter term provides a cut-off by penalizing a thinning of the film below a positive thickness threshold given by the minimum h_* of the potential. This is illustrated in Fig. 1, depicting $W(h)$, which also shows a sketch of a portion of a ridge as it dewets in the x-direction from a straight front oriented in y-direction. We let d_{SiO} be the thickness of the SiO layer and d_{OTS} the thickness of the monolayer of OTS.

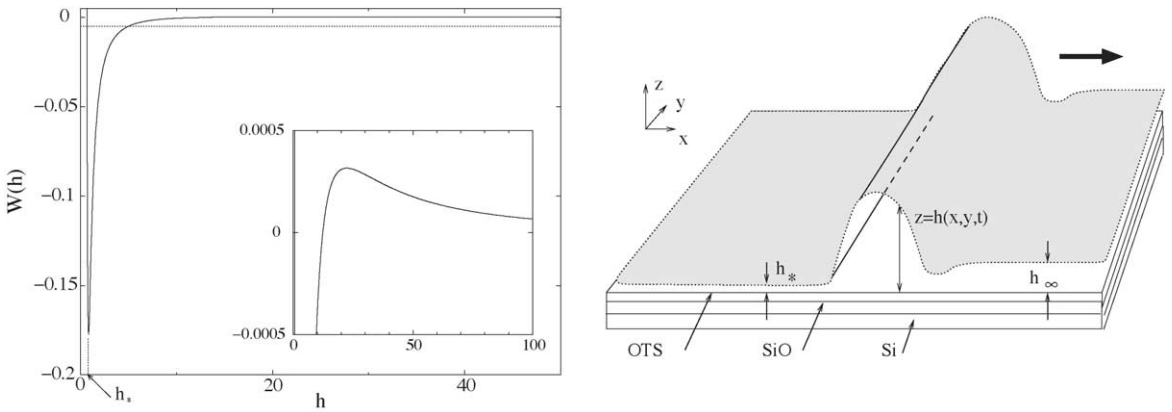

Fig. 1. Left: The non-dimensional effective interface potential $W(h)$, as given by (7), with a minimum at h_* and a maximum as shown in the inset. The inset corresponds to the area above the thin dotted line in the main figure. Right: Sketch of a portion of a dewetting polymer film of initial thickness h_∞. The dewetting front and the ridge propagate in the direction of the positive x-axis, as indicated by the bold-face arrow, leaving behind a residual film of thickness h_*.

The effective potential for this situation is (see [32]):

$$W(h) = \frac{c_s}{h^8} - \frac{A_{ots}}{12\pi h^2} + \frac{A_{ots} - A_{sio}}{12\pi(h + d_{OTS})^2} + \frac{A_{sio} - A_{si}}{12\pi(h + d_{OTS} + d_{SiO})^2}. \tag{1}$$

where c_s denotes the strength of the short-range part of the potential, and A_{sio}, A_{Si} and A_{OTS} are the Hamaker constants of PS on SiO, Si and OTS, respectively. We note that the actual values of the constants A_{OTS} and A_{SiO} turn out to nearly cancel out, so we can neglect the third term in what follows. For this system, it has been observed experimentally, that after formation of holes and formation of a ridge at the dewetting fronts of the holes, the ridges destabilize into finger-type structures.

2.2. Lubrication model

While the instability is seen for radially symmetric as well as for straight dewetting fronts we focus here only on modeling the evolution of a straight dewetting front. In order to describe the evolution of the film surface $z = h(x, y, t)$, we use a lubrication model that includes the influence of surface tension and the effective interface potential W of the air/PS/OTS/SiO/Si layer. In this case the pressure at $z = h(x, y, t)$ is given by

$$p = \sigma\Delta h - W''(h). \tag{2}$$

Making use of the small length scale of h one can then derive the lubrication model from the Navier–Stokes equation in conjunction with conservation of mass. In dimensional form, the lubrication model is

$$3\eta\frac{\partial h}{\partial t} + \nabla \cdot [m(h)(\sigma\nabla\Delta h - W''(h)\nabla h)] = 0, \tag{3}$$

where η and σ are the liquid viscosity and the liquid surface tension, respectively, and $W''(h)$ is the second derivative of the effective interface potential with respect to the PS film thickness h. As a first approximation for the short chained (2–5 kg/mol) variants of PS, which has an entanglement length of ∼18 kg/mol, our lubrication model (3) treats the polymer film in its melt state as a Newtonian liquid, so that in particular viscoelastic effects are not assumed to be present in the model.

Also, $m(h)$ is a non-negative mobility coefficient, the form of which depends on the boundary conditions at the liquid/solid interface. A widely used condition relates the slippage velocity v of the liquid at the wall to the local

shear rate $\partial v/\partial z$ via

$$v = \beta \frac{\partial v}{\partial z}, \tag{4}$$

where the slip length β is defined as the distance below the interface at which the liquid velocity extrapolates to zero. Usually, the slip length is very small, on the order of ten to a few hundred nanometers for Newtonian liquids and it only becomes relevant in the immediate vicinity of the contact-line.

For the problem we consider here the situation is different. Liquid polymer films of the type considered here and of such small thickness may have slip lengths on the order of the thickness of the dewetting film itself or even larger, depending also on the roughness of the substrate. Thus, slippage becomes an essential factor in the physical model that has an important influence on the flow in the liquid bulk.

For the above slip boundary condition at the substrate, the mobility has the form $m(h) = h^3 + \beta h^2$ with a non-zero slip length. There are two limiting situations for our model. The no-slip boundary condition, which is obtained if $\beta = 0$, so that the mobility has the form $m(h) = h^3$. On the other hand, the limit $\beta \to \infty$ yields the mobility $m(h) = h^2$, after rescaling time with β. We will call it the slip-dominated case, or just slip case for short.

Finally, we non-dimensionalize our problem with the intent of minimizing the number of parameters that appear in the equation. We require the time derivative of h, the contribution from surface tension and the first terms in $W''(h)\nabla h$ to balance. This is achieved with the following choices

$$H = \left(\frac{144\pi c_s}{A_{SiO}}\right)^{(1/6)}, \quad L = 4\pi \left(\frac{81\sigma^3 c_s^2}{2\pi A_{SiO}^5}\right)^{(1/6)}, \quad T = \frac{288\pi^3\eta\sigma}{A_{SiO}^3}\left(\frac{324 c_s^5 A_{SiO}}{\pi}\right)^{(1/6)} \tag{5}$$

for the normal and parallel length scales and for the time scale. Introducing these scalings for h, x, y and for t we obtain

$$\frac{\partial h}{\partial t} + \nabla \cdot \left[m(h) \left(\nabla \Delta h - \left\{ \frac{1}{h^{10}} - \frac{1}{h^4} + \frac{a}{(h+d)^4} \right\} \nabla h \right) \right] = 0. \tag{6}$$

Note that in (6) the slip length β, which is contained in the mobility $m(h)$, has also been scaled with H. The expression in curly brackets is the second derivative of the following non-dimensional form of the effective interface potential,

$$W(h) = \frac{1}{72h^8} - \frac{1}{6h^2} + \frac{a}{6(h+d)^2}, \tag{7}$$

which contains two parameters, namely

$$a = \frac{A_{SiO} - A_{Si}}{A_{SiO}} \qquad \text{and} \qquad d = \frac{d_{OTS} + d_{SiO}}{H}. \tag{8}$$

2.3. Nonlinear curvature

The OTS layer used in the experiments is very hydrophobic towards PS so that this system produces a contact angle of almost 60°, see [32]. Therefore, we also consider nonlinear curvature, replacing the linearized expression in (6), but otherwise retaining the usual terms contributing to the lubrication model in the liquid bulk. This is not strictly asymptotically correct, but has lead to reasonable results in other geometrically related situations, see for example [3]. This means, for comparison, we also investigate the model

$$\frac{\partial h}{\partial t} + \nabla \cdot [m(h)(\nabla \kappa - W''(h)\nabla h)] = 0, \tag{9}$$

where

$$\kappa(x, y, t) = \frac{(1+\rho^2 h_y^2)h_{xx} - 2\rho^2 h_x h_y h_{xy} + (1+\rho^2 h_x^2)h_{yy}}{(1+\rho^2(h_x^2+h_y^2))^{3/2}}, \tag{10}$$

with

$$\rho = \frac{H}{L} = \frac{1}{2}\left(\frac{A_{\mathrm{SiO}}^4}{18\pi^4\sigma^3 c_{\mathrm{s}}}\right)^{1/2}, \tag{11}$$

reducing to the linearized curvature for $\rho \to 0$. For easy reference, we will refer to (9) and (10) as the 'nonlinear curvature model', while we continue to use the term 'lubrication model' for (6).

3. Linear stability of the dewetting thin film

3.1. Non-constant base states

The base state about which will we perturb is in several ways non-constant in time. This is illustrated by Fig. 2(a), which shows a numerical solution of

$$\frac{\partial h}{\partial t} + \frac{\partial}{\partial x}\left[m(h)\left(\frac{\partial}{\partial x}\left(\frac{h_{xx}}{\left(1+\rho^2 h_x^2\right)^{3/2}}\right) - W''(h)\frac{\partial h}{\partial x}\right)\right] = 0. \tag{12}$$

at different times for the no-slip mobility $m(h) = h^3$, letting $\rho = 0$ to recover the lubrication model, i.e., the one-dimensional version of (6). Note that by using this one-dimensional model we consider here the evolution of trenches rather than of axisymmetric holes. The simulation starts with a slightly smoothed step function as initial profile that is also shown in the figure. One clearly sees that the dewetting ridge accumulates liquid as it moves to the right. As a consequence, the height as well as the width of the ridge increase. The simulations might suggest an approximately self-similar evolution of the ridge profile, but note that it connects to left and right far-field states that are constant in time and hence do not follow the scaling of the growing ridge.

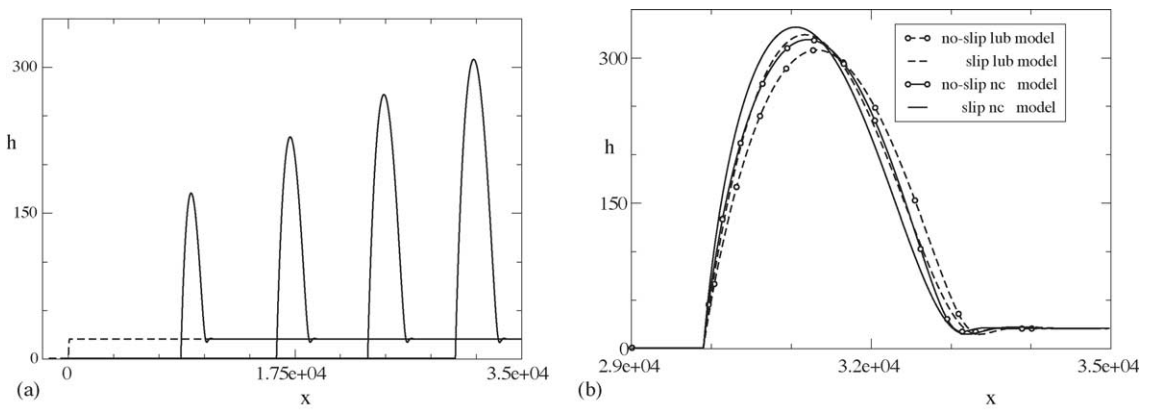

Fig. 2. (a) Evolution of the ridge profile for the no-slip lubrication model. The figures shows the initial profile (dashed line) and profiles at $t = 0.800\mathrm{e}6$, $0.160\mathrm{e}7$, $0.240\mathrm{e}7$ and $0.320\mathrm{e}7$, as solid lines in order from left to right. (b) The shape of the ridges after the contact-lines have travelled the same distance $x_{\mathrm{c}} = 2.99\mathrm{e}4$ for each of the four models. The abbreviations 'nc' and 'lub' are short for 'nonlinear curvature' and 'lubrication', respectively. We remark that the profile for the no-slip lubrication model coincides with the last profile in (a).

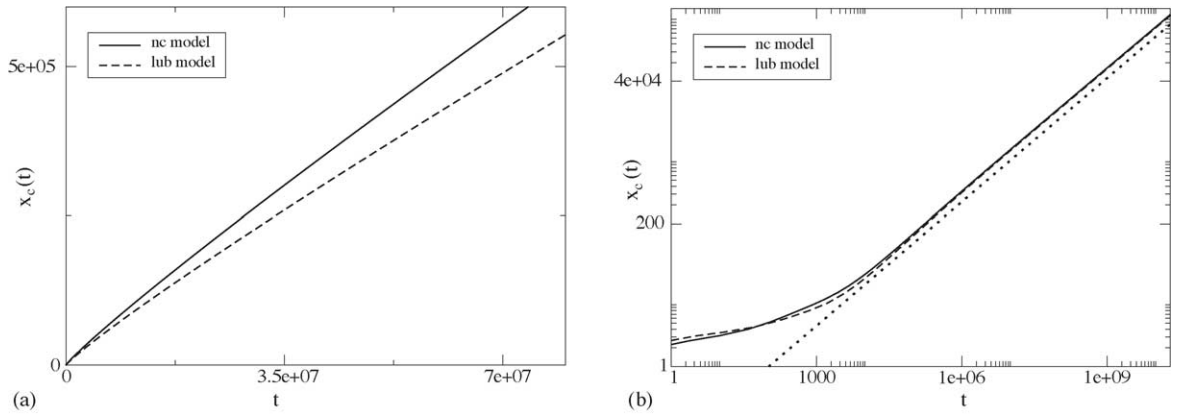

Fig. 3. Evolution of the contact-line position with time for the no-slip (a) and the slip case (b). A linear axis scaling is used for (a), while (b) is a log–log plot, where we have included a dotted line for the graph of $x \sim t^{2/3}$ to guide the eye.

The numerical results yield slightly different ridge shapes for the different models, i.e., with linear or nonlinear curvature (letting $\rho = 0$ or $\rho = H/L \neq 0$, respectively), and the no-slip or slip mobility. This is shown in Fig. 2(b), where we compare the ridge profiles after they have travelled the same distance, hence have accumulated the same amount of liquid. The profiles for the no-slip models have taller and thinner ridges than their slip counterparts. The same holds true for the nonlinear curvature models, i.e., the ridges are taller and thinner than those for the lubrication models ($\rho = 0$).

Further investigation of the receding ridge reveals that its velocity is non-constant and changes as the ridge evolves. The dewetting law depends on the boundary condition at the liquid/solid interface, which means it is different for the two mobilities considered in this paper.

In a similar setting like ours, [25] used energy balances to predict dewetting rates that are independent of the size of the receding ridge if no-slip boundary conditions are used at the contact-line, thus the ridge would move at a constant velocity. This result was corrected to a somewhat lower than linear dewetting law in [11,20] by numerical integration of the corresponding lubrication model. Also, it was found that an ansatz with a logarithmic correction could be excellently fit to the numerical solution found by integrating the lubrication and the nonlinear curvature model in one space dimension (12) for $m(h) = h^3$. The fit was in any case much better than with an ansatz assuming a linear time dependence for $x_c(t)$. Here $x_c(t)$ denotes the position of the front, and is taken to be the inflection point on the 'dry' side of the ridge, i.e., the side facing the region from which the liquid film has receded. A plot of the numerical solution is shown in Fig. 3(a), showing two curves for the nonlinear curvature and the lubrication model that are both close, but still visibly different, from a straight line.

For the slip case, when $m(h) = h^2$, [26,28] predict a $t^{2/3}$-law for the evolution of the dewetting front, which reads in scaled form using (5)

$$x_c(t) = \frac{3^{2/3} C^{1/3}}{4^{2/3}} \frac{\theta_s^{5/3}}{h_\infty^{1/3}} t^{2/3}, \qquad C \approx 0.1, \tag{13}$$

where θ_s is the static contact angle. By fitting a power-law ansatz, it was found in [20] that (13) indeed compares well with the numerical solution of (12) with mobility $m(h) = h^2$. This is also indicated by Fig. 3(b), where the contact-line evolution for numerical solutions of the nonlinear curvature and of the lubrication model is shown in a log–log plot. Clearly, $x_c(t)$ asymptotes to a straight line representing the graph of $\sim t^{2/3}$.

For the computations in Fig. 3 and all other computations presented below, we used the physical parameters given to us by Neto [23]:

$$c_s = 4 \times 10^{-81}\,\mathrm{Jm}^6, \quad A_{\mathrm{OTS}} = 2.2 \times 10^{-20}\,\mathrm{J}, \quad A_{\mathrm{Si}} = -1.4 \times 10^{-19}\,\mathrm{J},$$
$$d_{\mathrm{OTS}} + d_{\mathrm{Sio}} = 4.4 \times 10^{-9}\,\mathrm{m}, \quad \sigma = 30.8 \times 10^{-3}\,\mathrm{Nm}^{-1}. \tag{14}$$

The form of the potential is also found in [32], as well as the values for c_s and the Hamaker constants. In a further paper [31], Seemann et al. explain their method for determining these values in more detail.

The parameters in (14) lead to the length scales $H = 2.085 \times 10^{-10}$ m and $L = 1.290 \times 10^{-10}$ m, and for the non-dimensional parameters in the potential we get $a = 7.36$, $d = 21.1$. The viscosity and hence the time scale varies greatly for different chain lengths, moreover, it depends strongly on the temperature. Below we present our results for the stability analysis as a function of the dewetting front position, which does not require the knowledge of the time scale.

Note that the length scales are very small (in the sub-nanometric range) which is to be expected since the balance we used to fix them includes the Born repulsion term in the potential which acts only over very small scales. As a result, the minimum of the potential $h_* = 0.833$ (or 0.174 nm dimensionally) and hence the residual film thickness is an order one value in the scaled variables, while the size of the ridge or the distance it travels will be orders of magnitude larger. Recall that we chose this sort of inner scaling only with the intent to minimize the number of parameters in the PDE in order to facilitate numerical parameter studies. In particular, the length scale ratio $\rho = H/L > 1$ characterizes the contact-line region in the first place, while in the remaining regions (i.e., wet side of the ridge) the characteristic slopes are much smaller. This motivates our choice to retain the simplified bulk flow in conjunction with a nonlinear curvature term, as explained in Section 2.3.

The initial profile and in particular the initial thickness of the wetting film are the same as in Section 3.3.

3.2. The linearized problem

The stability analysis of a dewetting ridge we consider now is to some degree non-standard in that the base state about which we perturb is non-constant, nor does there seem to be an exact travelling wave or similarity solution. In the latter case, it would be possible to obtain a constant base state by the introduction of a co-moving frame of reference or similarity variables. Therefore, linearization about the base state does not lead to a problem that can be treated with the usual normal mode/eigenvalue ansatz. Normal modes can turn out to be insufficient for understanding stability/instability also if the linearized system is strongly non-normal, with eigenfunctions that are not orthogonal [7,37]. Such problems have found considerable attention in particular in the context of gravity driven thin film flow, see e.g. [1,9,12,13], which show considerable transient amplification of perturbations even where the eigenvalue analysis predicts stability, i.e., long-time decay of perturbations. However, in these problems the base state is constant in time, while the situation here is rather as in e.g. [39], where we have a base state that is non-constant in time and turns out to strongly amplifying small perturbations depending on their spanwise wavelength.

In what follows we describe the occurrence of fingers in the ridge, in terms of the evolution of a perturbation function $h_1(x, t)$. We introduce the perturbation

$$h(x, y, t) = h_b(x, t) + \delta h_1(x, t) \exp(iqy)$$

into the lubrication model, with $\delta \ll 1$ and retain only linear terms in δ. The curvature κ can then be written as

$$\kappa(x, y, t) = \kappa_b(x, t) + \delta\, \kappa_1(x, y, t)$$

where

$$\kappa_{\mathrm{b}}(x,t) = \frac{h_{\mathrm{b}xx}}{(1+\rho^2 h_{\mathrm{b}x}^2)^{3/2}} \tag{15}$$

and

$$\kappa_1(x,y,t) = \frac{h_{1xx} + (1+\rho^2 h_{\mathrm{b}x}^2) h_{1yy}}{(1+\rho^2 h_{\mathrm{b}x}^2)^{3/2}} - \frac{3\rho^2 h_{\mathrm{b}x} h_{\mathrm{b}xx}}{(1+\rho^2 h_{\mathrm{b}x}^2)^{5/2}} h_{1x}. \tag{16}$$

We obtain for the linearized equation

$$\frac{\partial h_1}{\partial t} + \mathcal{L}h_1 + \frac{\partial}{\partial x}\left[m(h_{\mathrm{b}}) \frac{\partial}{\partial x}\left(\frac{h_{1yy}}{(1+\rho^2 h_{\mathrm{b}x}^2)^{1/2}} \right) \right] + \frac{m(h_{\mathrm{b}})}{(1+\rho^2 h_{\mathrm{b}x}^2)^{1/2}} \frac{\partial^4 h_1}{\partial y^4} + m(h_{\mathrm{b}}) \frac{\partial^2}{\partial y^2}\left(\frac{h_{1xx}}{(1+\rho^2 h_{\mathrm{b}x}^2)^{3/2}} - \frac{3\rho^2 h_{\mathrm{b}x} h_{\mathrm{b}xx}}{\left(1+\rho^2 h_{\mathrm{b}x}^2\right)^{5/2}} h_{1x} - W''(h_{\mathrm{b}})\, h_1 \right) = 0, \tag{17}$$

where

$$\mathcal{L}h_1 = \frac{\partial}{\partial x}\left[m'(h_{\mathrm{b}}) \left(\kappa_{\mathrm{b}x} - W''(h_{\mathrm{b}})\, h_{\mathrm{b}x} \right) h_1 - m(h_{\mathrm{b}}) W'''(h_{\mathrm{b}}) h_{\mathrm{b}x} h_1 + m(h_{\mathrm{b}}) \times \left(\frac{\partial}{\partial x}\left[\frac{h_{1xx}}{\left(1+\rho^2 h_{\mathrm{b}x}^2\right)^{3/2}} - \frac{3\rho^2 h_{\mathrm{b}x} h_{\mathrm{b}xx}}{\left(1+\rho^2 h_{\mathrm{b}x}^2\right)^{5/2}} h_{1x} \right] - W''(h_{\mathrm{b}}) h_{1x} \right) \right] \tag{18}$$

We remark that by letting $\rho = 0$ in (17) and (18) and in the equation for the base state (9), we recover the system describing the linearization for the lubrication model.

Next, we Fourier-transform (17) and (18) with respect to y, which results in a system of spatially one-dimensional PDEs that depends on the span-wise wavenumber q. Note that since the coefficients of the linearized PDE are now non-constant, the solutions for the linearized problem cannot be obtained via a classical eigenvalue approach. Instead, we solve the initial value problems obtained from the linearisation numerically for a fixed set of wavenumbers, in tandem with the equation for the base state, and observe how the perturbations evolve in time. Both the equation for the base state (12) and the equation for the perturbation (17) coupled to it were discretized using a finite-difference scheme with implicit time discretisation, in some cases using the scheme proposed by [41]; this was also our approach for the linear curvature model.

3.3. Results of the linear stability analysis

The profile employed as initial condition for the base state is a steep front connecting the dewetted region, where the film thickness is h_*, and the unperturbed film of thickness h_∞, so that $\lim_{x\to-\infty} h = h_*$ and $\lim_{x\to\infty} h = h_\infty$. The initial front, specifically, its inflection point, is located at the origin. For the numerical experiments here, we usually set h_∞ to a reference value, $h_{\mathrm{ref}} = 20.8$ (noting in passing that this is $25h_*$). Recall that h_* is the film thickness that corresponds to the minimum of the potential (7) and is energetically strongly preferred compared to the initial thickness, so that in the computations the film dewets i.e., the front moves to the right.

An initial perturbation is introduced at a certain time t_0, defined below, using the following expression:

$$h_1(x,t_0) = \frac{\partial h_b}{\partial x}(x,t_0), \tag{19}$$

which corresponds to a 'zig–zag' perturbation, i.e., for a non-zero wave-number, we perturb both sides of the ridge in the same direction [5]. For zero wave-number, (19) simply represents an infinitesimal initial shift of the whole profile. Below, we also make some remarks on other choices of the initial data for h_1.

To describe the growth of bumps and eventually fingers in the ridges, we employ the amplification *A(t)* of the perturbation with respect to the initial state,

$$A(t) = \frac{\max_x |h_1(x,t)|}{\max_x |h_1(x,t_0)|} \qquad \text{for} \quad t_0 \le t \le t_1.$$

The evolution of the ridge profile happens on quite different time scales for the no-slip and the slip case, as can be expected, since the mobilities for the no-slip and the slip case differ by a factor of $h^3/h^2 = h$, which is typically on the order of, or larger than h_∞, in the ridge and the 'wetted' area. Therefore, we present the results of our stability analysis in terms of the position $x_c(t)$ of the dewetting front, rather than in terms of the dimensionless time t itself. In particular, we introduce the perturbation (19) in each of the four cases studied here (no-slip/slip, lubrication/nonlinear curvature model) when $x_c(t)$ has reached a fixed position equal to 26.7. This leads to four different values for t_0, one for each case. Then, the evolution of the base state and the perturbation coupled to it are followed until $x_c(t_1) = 4.5 \times 10^5$, which again specifies a different value for t_1 in each of the cases.

In the literature, the different dewetting rates for the no-slip and the slip case are typically derived from estimates of the energy dissipation rates that are independent from the size of the ridge for the no-slip but not for the slip situation. This results in a constant contact-line velocity in the former case, and a velocity that is inversely proportional to the width of the ridge in the latter, see for example [29], and references therein. The numerical results for the lubrication/nonlinear curvature model have confirmed these laws for the slip mobility, and also to some degree for the no-slip mobility, for which the less than linear law for $x_c(t)$ suggests some dependence of the dewetting rate on the size of the ridge. Nevertheless, it is reasonable to conclude that the dependence is much weaker than for the slip case.

This observation is potentially important, because it has been invoked as a possible explanation for how slip can promote the formation of protrusions in dewetting experiments [29]. In their article, Reiter and Sharma argue that if the dewetting velocity depends on the width of the rim, thicker regions in a perturbed ridge will tend to dewet more slowly than thinner regions, thus reinforcing the differences in the contact-line position. This could eventually lead to a pattern of protruding bumps or fingers separated by straight portions or by troughs like those observed in the physical experiment.

We now present the results for the linear stability analysis. Fig. 4 displays $A(t)$ versus the front position $x_c(t)$ for several wavelengths $l = 2\pi/q$, for the no-slip and the slip case, and for both the lubrication and the nonlinear curvature model. In all these cases and for each of the depicted wavelengths, the perturbation grows as the dewetting proceeds, then it reaches a maximum, after which it decays. Longer wavelengths achieve the maximal amplification factor

$$A_{\max} := \max_{t \ge t_0} A(t)$$

at later stages of the dewetting, when the front has advanced further into the film and the ridge of the base state has grown in size, suggesting that the most amplified wavelength correlates with the width of the ridge [19]. This coincides interestingly with results on fingering in gravity and Marangoni-driven flows, where the most amplified wavelength in the modal analysis is proportional to the length scale imposed by the bump width [38], and with predictions for the breaking up of static ridges [5] into droplets.

Comparing now the no-slip and the slip situation, we find that for a given wavelength, the maximum $A_{\max}$ is achieved earlier in the no-slip case, i.e., at a smaller value of x_c. More importantly, the value of $A_{\max}$ is lower, by up to several orders of magnitude, than for the slip scenario. This suggests that with slippage, the dewetting front is orders of magnitude more susceptible to span-wise perturbations of the front. We also compare, with slip and

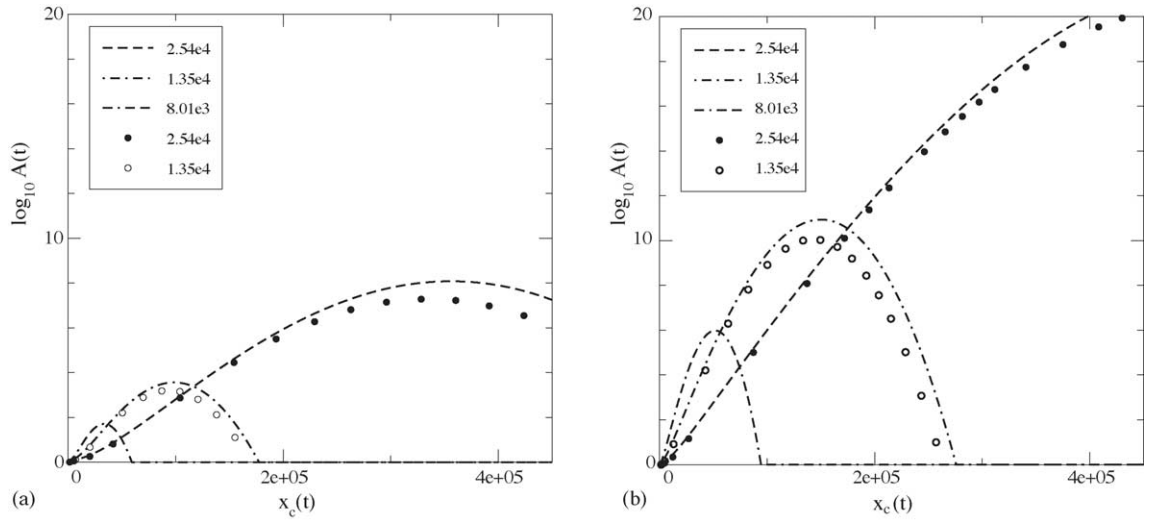

Fig. 4. Amplification $A(t)$ of the perturbation versus front position $x_c(t)$ (a) for the no-slip ($m = h^3$) and (b) for the slip case ($m = h^2$). Line styles correspond to different span-wise wavelengths as indicated in the legend, and represent the results for the model using nonlinear curvature. For the model with linear curvature, we include the curves for two wavelengths, using open and solid circles.

with no-slip, the amplification factors for the lubrication and the nonlinear curvature model, shown in Fig. 4. The amplification factor for the latter seem to be slightly larger, but this difference is small and becomes apparent only when the growth is about to saturate.

Fig. 5 shows profiles of the perturbation h_1 at different stages of amplification for both the no-slip (a) and the slip case (b) and highlights a characteristic property. In the no-slip case, the initial perturbation (given by (19)), which has one pronounced maximum and a minimum, rapidly evolves into a new profile where the minimum is replaced by a 'bump' which becomes a second maximum when $A(t)$ reaches its maximum value $A_{\max}$. To indicate how the

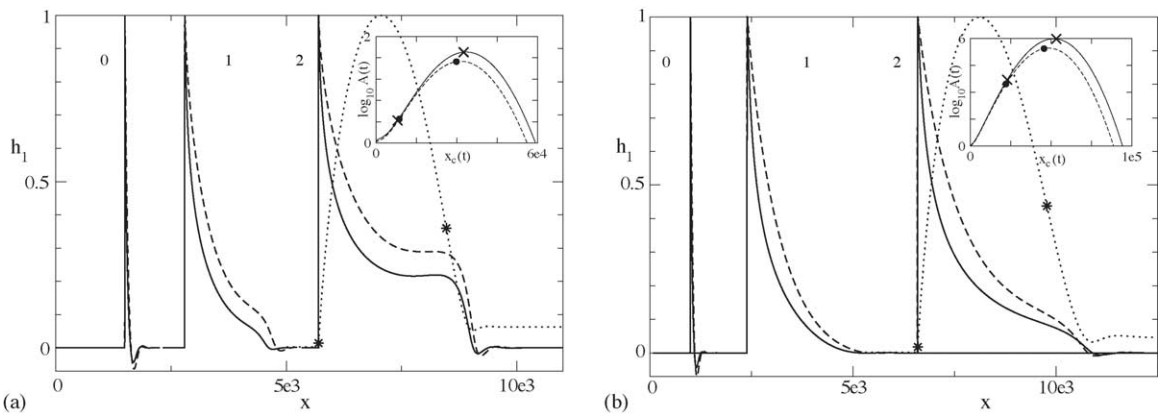

Fig. 5. Perturbation profiles h_1 for wave length $l = 8.01 \times 10^3$, for the no-slip case (a) and the slip case (b) at different positions x_c of the front in the base profile. The profiles for h_1 have been normalized so that their maximum is one, and shifted along the x-axis, for easier comparison (i.e., they are not in their true positions). For each subfigure, the perturbation profiles are labelled 0, 1 and 2, where label 0 denotes the initial perturbation introduced at t_0. Label 1 and 2 correspond to the front position/amplification factor given by the left and right cross (or circle) in the inset, respectively. Solid lines and crosses are used for the results for the nonlinear curvature model, while dashed lines and circles represent the results for the lubrication model. Further explanations are given in the text.

h_1 is aligned with h_b, we include the base state for the nonlinear curvature model as a dotted line in the figure. The height of the base profile has been rescaled by $\max h_b(x, t)$ so that it fits into the figure. The maxima of h_1 are located at the two sides of the ridge near the inflection points of the base state, which are marked by stars. This means that when the perturbation $\delta h_1(x, t)\cos(qy)$, i.e., the real part of $\delta h_1(x, t)\exp(iqy)$, is added to $h_b(x, t)$, both the front and the back side of the ridge are perturbed, in such a way that where $\cos(qy) > 1$, the 'dry' side of the ridge is shifted to lower x, while the 'wet' side is shifted to larger x, and vice-versa for $\cos(qy) < 1$. Thus, a ridge that is perturbed in this way will consist of a sequence of thicker and thinner portions reminiscent of a varicose or 'peristaltic' mode leading to the breakup of static ridges [5].

Conversely, for the slip case, the minimum fades out much more slowly and even for the perturbation profile at maximum amplification $A(t) = A_{\max}$, we only have a small 'bump' in the position where the no-slip case has a second maximum. Thus, with slippage, the perturbation hardly affects the 'wet' side of the ridge, meaning that the ridge stays relatively flat there; undulations would appear asymmetrically, i.e., mainly on the 'dry' side of the ridge. As for the no-slip case, the rescaled base state for the nonlinear curvature model has been included as a dotted line. Also, the inflection points on each side of the ridge are emphasized by stars. We confirmed in separate computations for the lubrication model that the typical shape of the perturbation profile, hence the asymmetric manner in which it affects the 'dry' and 'wet' side of the ridge, are obtained in the slip case also for different initial data. For each of our choices for $h_1(x, t_0)$, the perturbation profile quickly relaxed into the shapes shown in Fig. 5(b).

4. Conclusions

We investigated the lubrication model and an extended model that includes the full nonlinear curvature, describing the dewetting process of a thin polymer film on a hydrophobized substrate. The model assumed the dewetting process is driven by Van-der-Waals forces and either a no-slip or a slip-dominated condition for the mobility. We showed that the receding, slowly increasing ridge at the border of each trench strongly amplifies small span-wise perturbations. Interestingly, our analysis of the equations linearized about the non-constant base state shows that the amplification rate is by several orders of magnitude larger for the slip-dominated case than for the no-slip case for both the lubrication model and the extended model. Moreover, by comparing the perturbation profiles $h_1(x, t)$, we found that in the no-slip case the profiles develop two maxima, one on the front side towards the trench and the other one on the back side towards the thin film, while for the slip case only one maximum on the front side develops. The means that the slip case would show asymmetric protrusions extending towards the trench, while for the no-slip case the protrusions are symmetrical.

Finally we want to make some remarks on preliminary results regarding the wavelength of the most amplified perturbations. First, we adapted our code for the dynamic base state to determine the fastest growing wavelength for a static ridge of height h_{ref}. The wavelength was about four times the width of the ridge measured between the two inflection points, with a slightly larger ratio for the nonlinear curvature model. This agrees with values given in [5].

To find out whether such a relation between width of ridge and preferred wavelength holds, we performed some preliminary computations for the dewetting ridge, where we divided the wavelength $l = 2\pi/q$ by the width of the ridge at which either the amplification factor or the growth rate $\dot{A}(t)$ becomes maximal, and found that the numerical values obtained for each of these ratios hardly changed for different choices of the wavenumber q. We note that we took twice the distance of the front (i.e., the inflection point) from the maximum of the ridge as a measure for the width of the ridge, and also that we restricted this part of our investigation to the slip case. For the lubrication model and wavelengths $l = 13.5 \times 10^3, 8.01 \times 10^3$ and 5.00×10^3, the maximum amplification factor was achieved when the ratio of wavelength and width was equal to 2.5; at the time of maximal growth rate—which occurred earlier—we obtained values in the range 2.75 ± 0.1. For the nonlinear curvature model, these values were only slightly larger, up to about 10%. For both models the corresponding values do not differ much if larger wavelengths are taken into

consideration. This suggests that there could be limiting values for these ratios as the wavelengths increase. We are currently investigating these trends further.

Acknowledgements

AM was supported in part by the DFG grant MU 1626/2-1 and a Heisenberg scholarship, and by the DFG Research Center MATHEON. The authors thank Chiara Neto, Karin Jacobs, Ralph Seemann, Tom Witelski, Ralph Blossey for helpful discussions.

References

[1] A.L. Bertozzi, M.P. Brenner, Linear stability and transient growth in driven contact-lines, Phys. Fluids 9 (3) (1997) 530–539.
[2] A.L. Bertozzi, A. Münch, X. Fanton, A.M. Cazabat, contact-line stability and 'undercompressive shocks' in driven thin film flow, Phys. Rev. Lett. 81 (23) (1998) 5169–5172.
[3] M.P. Brenner, D. Gueyffier, On the bursting of liquid films, Phys. Fluids 11 (3) (1999) 737–739.
[4] F. Brochard-Wyart, P.-G. de Gennes, H. Hervert, C. Redon, Wetting and slippage of polymer melts on semi-ideal surfaces, Langmuir 10 (1994) 1566–1572.
[5] F. Brochard-Wyart, C. Redon, Dynamics of liquid rim instabilities, Langmuir 8 (1992) 2324–2329.
[6] J.B. Brzoska, F. Brochard-Wyart, F. Rondelez, Exponential growth of fingering intabilities of spreading films under horizontal thermal gradients, Europhys. Lett. 19 (1992) 97–102.
[7] K.B. Butler, B.F. Farrell, Optimal perturbations and streak spacing in wall bounded shear flow, PoF A 5 (1993) 774.
[8] A.M. Cazabat, F. Heslot, S.M. Troian, P. Carles, Finger instability of this spreading films driven by temperature gradients, Nature 346 (6287) (1990) 824–826.
[9] J.M. Davis, S. Troian, On a generalized approach to the linear stability of spatially nonuniform thin film flows, PoF 15 (2003) 1344.
[10] N. Garnier, R.O. Grigoriev, M.F. Schatz, Optical manipulation of microscale fluid flow, Phys. Rev. Lett. (2003) 91 (Art. No. 054501).
[11] A. Ghatak, R. Khanna, A. Sharma, Dynamics and morphology of holes in dewetting of thin films, J. Colloid Interface Sci. 212 (1999) 483–494.
[12] R. Grigoriev, Transient growth in driven constact lines. Physica D, this issue (2004).
[13] K.-H. Hoffmann, B. Wagner, A. Münch, On the generation and spreading of finger instabilities in film coating processes, Lect. Notes Comp. Sci. Eng. 8 (1999) 245–254.
[14] H. Huppert, Flow and instability of a viscous current down a slope, Nature 300 (1982) 427–429.
[15] K. Jacobs, R. Seemann, G. Schatz, S. Herminghaus, Growth of holes in liquid films with partial slippage, Langmuir 14 (1998) 4961–4963.
[16] D.E. Kataoka, S.M. Troian, A theoretical study of instabilities at the advancing front of thermally driven coating films, J. Colloid Interface Sci. 192 (1997) 350–362.
[17] R. Konnur, K. Kargupta, A. Sharma, Instability and morphology of thin liquid films on chemically heterogeneous substrates, Phys. Rev. Lett. 84 (5) (2000) 931–934.
[18] P.G. López, S.G. Bankoff, M.J. Miksis, Non-isothermal spreading of a thin liquid film on an inclined plane, J. Fluid Mech. 11 (1996) 1–39.
[19] J.-L. Masson, O. Olufokunbi, P.F. Green, Flow instabilities in entangled polymer films, Macromolecules 35 (2002) 6992–6996.
[20] A. Münch, Dewetting rates of thin liquid films, J. Phys.: Condensed Matter (2004).
[21] A. Münch, C. Neto, R. Seemann, K. Jacobs, Fingering instability in dewetting films induced by slippage, in preparation.
[22] A. Münch, B.A. Wagner, Numerical and asymptotic results on the linear stability of a thin film spreading down a slope of small inclination, Eur. J. Appl. Math. 10 (1999) 297–318.
[23] C. Neto, Private Communications.
[24] C. Neto, K. Jacobs, Physica A, submitted for publication.
[25] C. Redon, F. Brochard-Wyart, F. Rondelez, Dynamics of dewetting, Phys. Rev. Lett. 66 (6) (1991) 715–718.
[26] C. Redon, J.B. Brzoska, F. Brochard-Wyart, Dewetting and slippage of microscopic polymer films, Macromolecules 27 (1994) 468–471.
[27] G. Reiter, Dewetting of thin polymer films, Phys. Rev. Lett. 68 (1) (1992) 75–78.
[28] G. Reiter, R. Khanna, Kinetics of autophobic dewetting of polymer films, Langmuir 16 (2000) 6351–6357.
[29] G. Reiter, A. Sharma, Auto-optimization of dewetting rates by rim instabilities in slipping polymer films, Phys. Rev. Lett. 80 (16) (2001).
[30] G. Reiter, A. Sharma, A. Casoli, M.-O. David, R. Khanna, P. Auroy, Thin film instability induced by long-range forces, Langmuir 15 (1999) 2551–2558.

[31] R. Seemann, S. Herminghaus, K. Jacobs, Dewetting patterns and molecular forces: a reconciliation, Phys. Rev. Lett. 86 (24) (2001) 5534–5537.
[32] R. Seemann, S. Herminghaus, K. Jacobs, Gaining control of pattern formation of dewetting films, J. Phys.: Condensed Matter 13 (2001) 4925–4938.
[33] A. Sharma, R. Khanna, Pattern formation in unstabile thin liquid films, Phys. Rev. Lett. 81 (16) (1998) 3463–3466.
[34] A. Sharma, R. Khanna, Pattern formation in unstable thin liquid films under influence of antagonistic short- and long-range forces, J. Chem. Phys. 110 (10) (1999) 4929–4936.
[35] A. Sharma, G. Reiter, Instability of thin polymer films on coated substrates: rupture, dewetting and drop formation, J. Colloid Interface Sci. 178 (1996) 383–389.
[36] N. Silvi, E.D.V. On the rewetting of an inclined solid surface by a liquid. Phys. Fluids, 28 (1985) 5–7.
[37] L.N. Trefethen, A.E. Trefethen, S.C. Reddy, T.A. Driscoll, Hydrodynamics stability without eigenvalues, Science 261 (1993) 578.
[38] S.M. Troian, E. Herbolzheimer, S.A. Safran, J. Joanny, Fingering instabilities of driven spreading films, Europhys. Lett. 10 (1) (1989) 25–30.
[39] M.R.E. Warner, R.V. Craster, O.K. Matar, Fingering phenomena associated with insoluble surfactant spreading on thin liquid films, JFM 4510 (2004) 169–200.
[40] R. Xie, A. Karim, J.F. Douglas, C.C. Han, R.A. Weiss, Spinodal dewetting of thin polymer films, Phys. Rev. Lett. 81 (6) (1998) 1251–1254.
[41] L. Zhornitskaya, A.L. Bertozzi, Positivity preserving numerical schemes for lubrication-type equations, SIAM J. Numer. Anal. 37 (2) (2000) 523–555.